RESEARCH ARTICLE

Initial Propulsion System Study for the Futuristic Hyperloop Transportation System: Design, Modeling, and Hardware in the Loop Verification

MOHAMMAD ABDUL BHUIYA[1,2], (Member, IEEE), AND MOHAMED Z. YOUSSEF[3], (Senior Member, IEEE)

[1]ECSE Department, Ontario Tech University, Oshawa, ON L1G 0C5, Canada
[2]General Dynamics Land Systems (GDLS), London, ON N5V 2Z7, Canada
[3]Department of Engineering and Applied Science, Oshawa, ON L1G 0C5, Canada

Corresponding author: Mohamed Z. Youssef (mohamed.youssef@ontariotechu.ca)

ABSTRACT Recently, the proposal for a futuristic mode of transportation known as the Hyperloop has been popularized. Currently, there are only some reports regarding the design of the Hyperloop. More specifically, reports regarding the propulsion system design methodology for Hyperloop is minimal. Thus, this paper provides an initial steppingstone to modeling and simulation study for the propulsion system in a Hyperloop. The main contribution of this study is to provide a relatively simple design methodology for any future Hyperloop endeavors. This is shown using state of the art simulators to aid in designing the propulsion system. The design revolves around the linear synchronous motor based on field-oriented control through a three – phase inverter. PSIM is used to develop the model and design the full power system and controller. This includes the DC-DC converter, battery system model, three – phase inverter, and the motor controller. The motor used for modelling is a rotary permanent magnet synchronous motor. Finally, hardware in the loop technology is used to verify and validate the design. The controller design is tested through a Texas Instrument digital signal processor. The real time verification shows matching results with the offline simulation model.

INDEX TERMS Hyperloop, three—phase inverter, field—oriented control, propulsion system, linear synchronous motor, electrification, power electronics, PSIM, simulink, typhoon HIL.

I. INTRODUCTION

Today's society faces vast engineering challenges. These challenges are crucial for the growth of the world economy. The rise of the electric vehicle industry has greatly impacted other sectors of the industry. More companies are starting to follow the trend to a better and secure future. Moreover, energy security is a reoccurring issue that needs to be addressed. Industries are researching and developing environmental conscious solutions. Corporations such as Hyperloop One and Transpod are investing heavily on a new electric mode of transportation that can revolutionize the industry. This proposed mode transportation, known as the Hyperloop, will be key in solving many problems society faces today. Thus, furthering the goals for a better

world. SpaceX presented the Hyperloop concept in a white paper. Goals for the proposed system requires a significant improvement in various methods of transportation compared to current systems. Considerations for improvement include safety, speed, cost, sustainability, convenient, etc. [1]. The proposed Hyperloop system requires complex engineering design concepts, combining various aspects of current technology and iterative improvements. There are various parts of the Hyperloop system that requires its own research and development for the system to work to its full potential. These various parts include the design of the pod (which includes design considerations such as compressor, suspension, onboard power, propulsion, etc.), tube design, propulsion, and levitation systems (combining both pod components and tube components), etc. In this research, a few of these design challenges were studied, modeled, and integrated. The study addresses various design challenges in the power and

The associate editor coordinating the review of this manuscript and approving it for publication was Jie Gao ![ORCID].

control stages for the overall Hyperloop system. The topic of Hyperloop has been reported in various literature works such as [2] and [3]. The work in [2] critiques the achievability by discussing the technical issues in building such an infrastructure. Based on their calculations, they estimate for a Hyperloop pod traveling at 1200 km/h for an estimated weight of 26 000 kg would require 689 kW of power. Additionally, they estimate that the cost for building the Hyperloop infrastructure in Poland (including design, construction, land, etc.) for distances between 3000 – 30 000 km would cost over $50 billion. In [3], the authors discuss the electric power requirements for a full scale Hyperloop. They estimate for a large freight, a capacity of 58 000 lb would be

required for the pod. The paper also estimates a cruise speed of 1012 km/h with 80 % regenerative braking efficiency. The resulting power usage is estimated to be in the megawatt range (820 – 1980 MW). The grid assessment for an integrated Hyperloop system showed high pulsating load profiles. Which could result in high excess of voltage fluctuation, flickering, and large disturbances. A solution the authors provide is using compensation devices (static compensators and static var compensators). Another viable solution they provide is the use of energy storage devices in unison with the grid. As mentioned above, two types of linear motors are commonly studied regarding propulsion of maglev trains. Linear induction motors are attractive due to their relatively low cost and complexity. However, compared to the linear synchronous motor (LSM), their power factor is low and because it is not a synchronous machine, the design must include slip. Therefore, the LIM has a lower energy efficiency [4], [5]. Despite the cost and complexity, the linear synchronous motor has various properties that makes it a desirable choice for a maglev motor. The LSM has been reported in various papers such as [6], to be viable solutions for a Hyperloop propulsion system. LSM allows the vehicle to avoid carrying heavy traction motor on board. This is because LSM supplies the traction power by supplying it through the ground coils on the guideway [7]. Moreover, this allows transformers and inverter systems to be on ground rather than on board. Accordingly, the pod system will be significantly lighter allowing for faster speeds. Another outcome would be that the pantograph - catenary can be avoided, reducing concerns regarding mechanical contact problems at high speeds [7]. The study in [8] found that coreless, permanent magnet linear synchronous motor (PM- LSM) can achieve promising results for a relatively low cost. Comparing the LIM and the PM-LSM, the LSM had an efficiency of 95.17% compared to the LIM, which had an efficiency of 17.18%. The power factor of the LSM achieved unity, whereas the LIM had a low value of 0.814 [8]. Although the LSM has greater efficiencies and power factor, the LIM is still a popular choice for many linear motor propulsion systems. This is mainly chosen of the LSM because of the significant infrastructure costs. The study in [9] presents various LIM and LSM data regarding costs, efficiencies, and speed capabilities. They conclude similar findings like the other reports that LIM is a significantly better

TABLE 1. General design parameter for the hyperloop system.

Propulsion	Costs	Efficiency at maximum speeds	Operational Speed
LIM	$23 million/km	77%	100 km/h or less
LSM	$50 million/km	87%	200 km/h or more

economical choice at low speeds. Table 1 summarizes some of the metrics for deciding on the propulsion motor. Although this is a very simplistic cost analysis, it is still presented for an initial design choice. At first glance, the obvious choice would be the linear induction motor. The cost difference vs the efficiency is significantly siding towards the LIM. However, the LIM's natural limitation of its speed is huge drawback for Hyperloop applications. To obtain ultra-high speeds, the LSM is clearly the only viable choice currently. Moreover, the increase in efficiencies with the LSM may present a case for a reasonable return on investment.

To simulate the proposed Hyperloop propulsion system, an accurate mathematical model for the LSM is required. This will allow a better study on the dynamic behaviour of the physical LSM system. Various papers such as [10], study the control algorithms of AC motors using the d-q axes model. A dynamic model of an ironless Halbach permanent magnet linear synchronous motor (PMLSM) is presented in [11]. The model is derived using synchronous reference frame (d-q). The paper in [12] presents a mathematical model for a long stator linear synchronous motor (LLSM) in d-q reference frame and converts it into two phase stationary coordinate system (alpha – beta). In [13] and [14] modeling of PMLSM was developed in MATLAB using the d-q reference frame. The research in [15] develops a LLSM in MATLAB for hardware in the loop integration. To develop the control for the Hyperloop propulsion system, vector control is commonly used. The study in [16] develops electromagnetic thrust and levitation force using two – phase rotating reference frame for a PMLSM. The maglev PMLSM has two independent stator windings (one for thrust and the other for suspension). The pod acts as rotor with permanent magnets arranged in the Halbach array. The study simulates the RFOC (rotor field-oriented control) of PMLSM in PSIM. The proposed FOC scheme uses two closed loops. It includes an outer PI speed controller and an inner PI current controller. The FOC system requires three sensor values (current, position and speed). Additionally, the study dives into minimum switching loss SVPWM method. The motivation for this was because conventional SVPWM cannot effectively reduce losses and harmonics. Sensor-less control has been an emerging area of research for maglev systems. The paper in [17] states the drawbacks from using magnetic encoders (to obtain position and speed values). It mentions that the cost of encoders will be high as they will be required to be installed across the long stator. This brings in issues regarding maintenance. And lastly, encoders are restricted by environmental factors

TABLE 2. General design parameter for the hyperloop system.

| PARAMETER	VALUE
Total pod mass (mp)	mp = 15000 [kg]
Steady state velocity (Vconst)	Vconst = 300 [m/s]
Acceleration (a)	a = 1.96 [m/s2] (i.e. 0.2G)
Deceleration (d)	d = 1.96 [m/s2] (i.e. 0.2G)
Distance (s)	s = 615 [km]

(e.g. temperature, humidity, vibrations). The paper presents a disturbance observer based senseless control system for linear permanent magnet motors. The basis of the system uses back EMF observers and a phase locked loop to estimate the position. The performance of the sensor-less control system was on par with the actual encoder. The proposed Hyperloop system requires complex engineering design concepts, combining various aspects of current technology and iterative improvements. There are various parts of the Hyperloop system that requires its own research and development for the system to work to its full potential. Some of these various parts include the design of the pod (e.g. compressor, suspension, onboard power, aerodynamics, etc.), vacuum tube design, propulsion, and levitation systems, etc. In this research, a few of these design challenges were studied, modeled, and integrated. The study addresses various design challenges in the power and control stages for the overall Hyperloop system. More specifically, the study dives into the propulsion system. The concepts of levitation and propulsion systems are borrowed from existing maglev technology. However, this technology is still new and continuously developing. Further research to improve the maglev's drive system will be very beneficial for the propulsion system designed specifically for the Hyperloop. The study hopes to provide a steppingstone for future implementation and prototyping designs.

II. SYSTEM MODELING AND ENGINEERING DESIGN

The models discussed in this section will be implemented in pair with PSIM and Typhoon HIL to validate and verify the integration of the models. Assumptions and reference design from various sources were made to determine design parameters such as mass, speed, acceleration, etc. These parameters are later used to model the system and study the simulated results. The basic design parameters for the proposed Hyperloop modeling are given in Table 2.

A. LINEAR SYNCHRONOUS MOTOR

In an LSM based Hyperloop system, we have the track (stationary part) and the pod (moving part). The speed of the moving part can be calculated using (1). Where, v_s is the synchronous speed, ω is the angular input frequency and τ is the pole pitch (in mm). The thrust force (output power divided
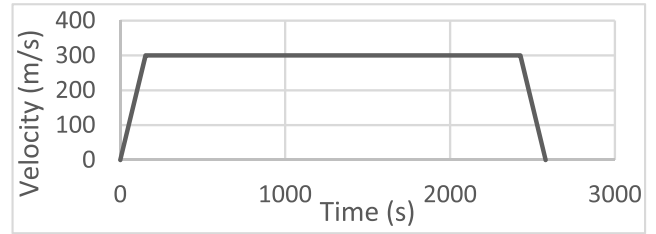
FIGURE 1. Calculated speed – time profile.

by the synchronous speed) can be calculated using (2)

$$v = v_s = 2f\tau = \frac{\omega}{\pi}\tau \tag{1}$$

$$F_x = \frac{P_{out}}{v_s} \tag{2}$$

The previous equations are used for basic motion calculation. Additionally, speed-time and thrust-time curves can be created for the linear motion. To solve for the linear motion waveforms the kinematic equations can be used. Based on the parameters in Table 1, we can model the speed-time curve given in Fig. 1.

The circuit model for the linear synchronous motor can be derived based on the rotary synchronous motor equations. The circuit model for the linear synchronous motor is presented in (3) – (15).

| Equation	Description	
$V_d = R_1 i_d + \frac{\partial \psi_d}{\partial t} - \omega_r \psi_q$	d - axis stator voltage	(3)
$V_q = R_1 i_q + \frac{\partial \psi_q}{\partial t} + \omega_r \psi_d$	q – axis stator voltage	(4)
$V'_F = R'_F i'_F + \frac{\partial \psi'_F}{\partial t}$	Field excited voltage	(5)
$\psi_d = L_{a1} i_d + L_{dm}(i'_F + i_d)$	d – axis flux component	(6)
$\psi_q = L_q i_q$	q – axis flux component	(7)
$\psi'_F = L_{F1} i'_F + L_{dm}(i'_F + i_d)$	Excitation linkage flux	(8)
$\frac{i'_F}{i_F} = \frac{M_{aF}}{L_{dm}} = K_F$	Field exited current	(9)
$V'_F = \frac{1}{K_F} V_F$	Field excited voltage	(10)
$\omega_r = \frac{\pi}{\tau} U$	Angular rotor velocity (angular frequency of the armature current)	(11)
$F_x = \frac{2}{3}\frac{\pi}{\tau}(L_{dm} i'_F + (L_{dm} - L_{qm})i_d)i_q$	Propulsion Force	(12)
$\frac{M}{2}\frac{dU}{dt} = F_x - F_{load}$	Acceleration equation	(13)
$L_d = L_{dm} + L_{a1}$	d – axis field leakage inductance	(14)
$L_q = L_{qm} + L_{a1}$	q – axis field leakage inductance	(15)
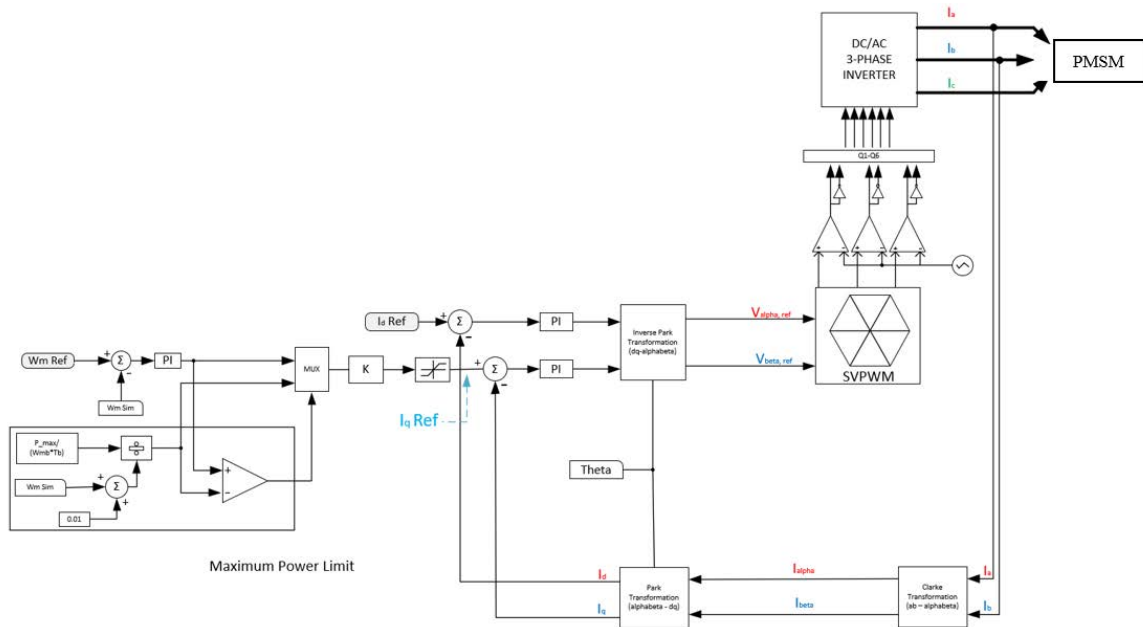
FIGURE 2. Field - oriented control algorithm (block diagram).

Vd,Vq are the stator voltages in the d and q axis, respectively. id and iq are the stator currents. R1 is the armature winding resistance. ψd, ψq are the flux components. The inductive windings are represented by Ld and Lq. Additionally, these inductances can be calculated as shown in (14) – (15). Where Ldm and Lqm are the magnetizing inductance. La1 is the leakage inductance. The angular frequency of armature current is represented by ωr (i.e. angular rotor velocity), where U is the linear synchronous velocity and the pole pitch is denoted as τ. In the case of electromagnetic excitation, there exists field winding resistance, R'f [18]. The variable i'f is the field excited current. ψf is the excitation linkage flux. L_{F1} represents the field leakage inductance.

The propulsion force can be calculated using (12). Equation (13) relates the mass (M), acceleration (a = dU/dt) and movement resistance force (Fload). M/2 represents the mass of one side of the vehicle powered by one inverter for one active stator section [19].

B. MODELING OF THE FIELD ORIENTED CONTROL

In motor controller design the d-q frame of reference theory is an important part of motor controller design. As a result, the phase values measured must be translated to the two-phase d-q axis. To do so, we must first take the two a, b phase currents and convert the signals into alpha-beta frame of reference. This is done by using the Clarke transformation. Next, the alpha-beta currents are then transformed into the desired dq currents using Park's transformation. A reference Id (flux reference) is assigned a fixed value and is compared to the transformed direct current Id. A Iq reference (torque reference) is compared to the transformed quadrature current (Iq). Using a speed controller, a calculation for this torque

reference can be made. As illustrated in Fig. 2, there are two components (speed regulator and maximum power limiter).

The machine's velocity (angular in the case of rotary PMSM) is measured and compared to a reference. Here, the reference velocity is a user-input command. The error signal for the speed is the output of the summer which is then sent to the PI regulator/controller. This regulator is popularly used in field-oriented control (FOC) as it regulates the torque and flux feedback well. The PI constants (K_{pi} and K_i) should be chosen correctly to reach steady state [20]. The output of the PI block is then used in two blocks, the multiplexer, and the maximum power limiter. The error signal at the speed controller gets converted to a torque value, which is limited to the maximum torque ($+T_{max}/T_b$ & $-T_{max}/T_b$). This value is used to compare (through the comparator) with the maximum power. The maximum power is divided by the measured velocity to obtain the electromagnetic torque. The compared value is sent to the multiplexer. The block determines the correct output depending on the selector's signal. After the multiplexer, the signal goes through a gain block to transform the torque value into a current value. The mathematical relationship of K ($1/(K_{TA} * i_b/T_{pu})$) is given in (16). Here, I_s represents space vector stator current and k_T represents the torque constant. Finally, this current value is limited by $\pm I_{qmax}$ which is given by (16). The output of the limiter is our I_q value.

$$I_s = \frac{T_{em}}{k_T} \qquad (16)$$

$$I_q^* = \sqrt{\hat{I}_s^2 - |I_d|^2} \qquad (17)$$

The next process of the FOC method is the current control. The calculated reference I_q and the measured I_q values are compared through a summer. The difference is taken,
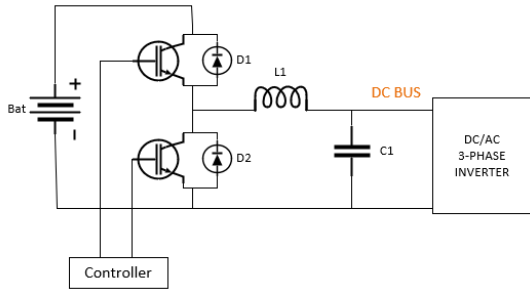
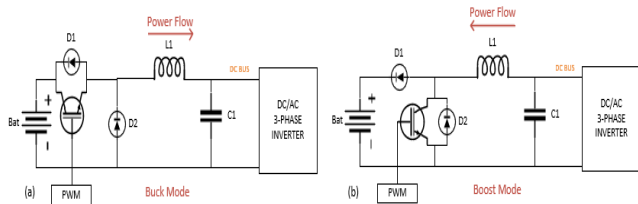**FIGURE 3.** Buck-type bidirectional DC-DC converter.

FIGURE 4. Bidirectional DC-DC converter in (a) buck mode operation & (b) boost mode operation.

providing the error signal of the quadrature current. Again, the error signal is placed into a PI block. This process is repeated for the direct current I_d. The output of the current regulators are the dq reference voltages. These voltages are transformed using inverse parks transformation to obtain the alpha beta reference voltages of the stator vector. The alpha beta voltages are in the stationary orthogonal reference frame, thus can be used in generation of pulse with modulation via the space vector PWM block. The switching pattern is generated by comparing the sinusoidal reference signal with the carrier wave.

C. MODELING OF THE REGENERATIVE SYSTEM

To model the regenerative system, we opted with a half bridge DC-DC bidirectional converter for a proof-of-concept model. This topology was studied in [21]. The buck-type bidirectional DC-DC converter is illustrated in Fig. 3. It consists of a lithium-ion battery, two IGBTs, an inductor and a capacitor. The bidirectional converter has two different modes of operation known as boost mode and buck mode. The buck mode operates when the motor is in the regeneration mode. Boost mode operates when the motor is in generation mode. The bidirectional converter shown can be operated in buck mode by turning off the lower leg IGBT, this will leave just the diode D2. The upper leg IGBT will be switched via PWM. The new converter can then be modeled as shown in Fig. 4. For boost mode of operation, the upper leg IGBT is turned off (leaving diode D1) and the lower leg IGBT is switched via PWM.

Design equations for the buck converter are presented in (18) – (20). The duty cycle given in (18), can be determined by taking the ratio of the output voltage over the input voltage, or the input current over the output current. The inductor
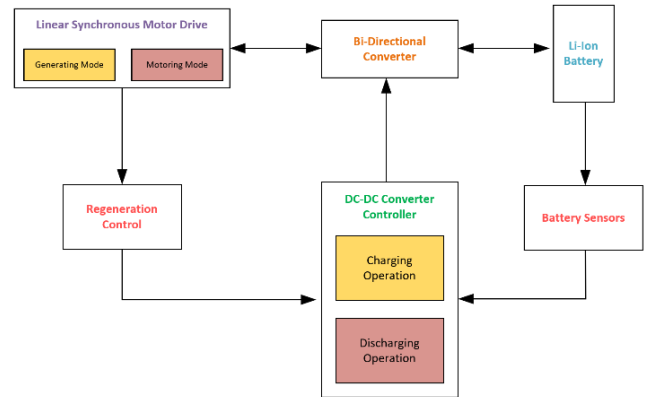

FIGURE 5. Bi-Directional DC-DC controller based on [22].

value can be calculated by using (19). The critical inductor value determines the point at which the converter works in continuous conduction mode (CCM). Depending on desired cost, size, and performance of the converter, the inductor value is equal to a multiple of the critical inductance. Finally, the capacitor value can be determined using (20) for a certain voltage ripple.

$$D = \frac{V_{out}}{V_{in}} = \frac{I_{in}}{I_{out}} \tag{18}$$

$$L_{crit} = \frac{(1-D)}{2}TR \tag{19}$$

$$\frac{\Delta V_c}{V_{out}} = \frac{(1-D)}{8LCf^2} \tag{20}$$

The equations used to design a boost converter is given in (21)-(23).

$$\frac{V_{out}}{V_{in}} = \frac{I_{in}}{I_{out}} = \frac{1}{1-D} \tag{21}$$

$$L_{crit} = \frac{RT}{2}(1-D)^2 D \tag{22}$$

$$\frac{\Delta V_{out}}{V_{out}} = \frac{D}{RCf} \tag{23}$$

Using digital logic, the function of the bidirectional converter can be controlled. In [22], the author presents a method to simulate a bidirectional DC-DC converter using charging, discharging and regenerative control blocks developed in PSIM. The block diagram shown in Fig. 5 represents the modeling of the controller for the Bi-Directional DC-DC system. The model works by first determining the state of the motor. If the LSM has a positive power (in terms of thrust and speed) then it is in motoring mode of operation, otherwise a negative power indicates braking mode. Therefore, by determining the speed and thrust force of the motor the controller can determine if the converter should be in buck or boost mode of operation. An additional state the controller looks at, before determining the course of action for the converter, is the state of the battery. Thus, the charging mode of operation occurs when $V_{batt} < V_{float}$ and the motor is in regenerative braking mode.
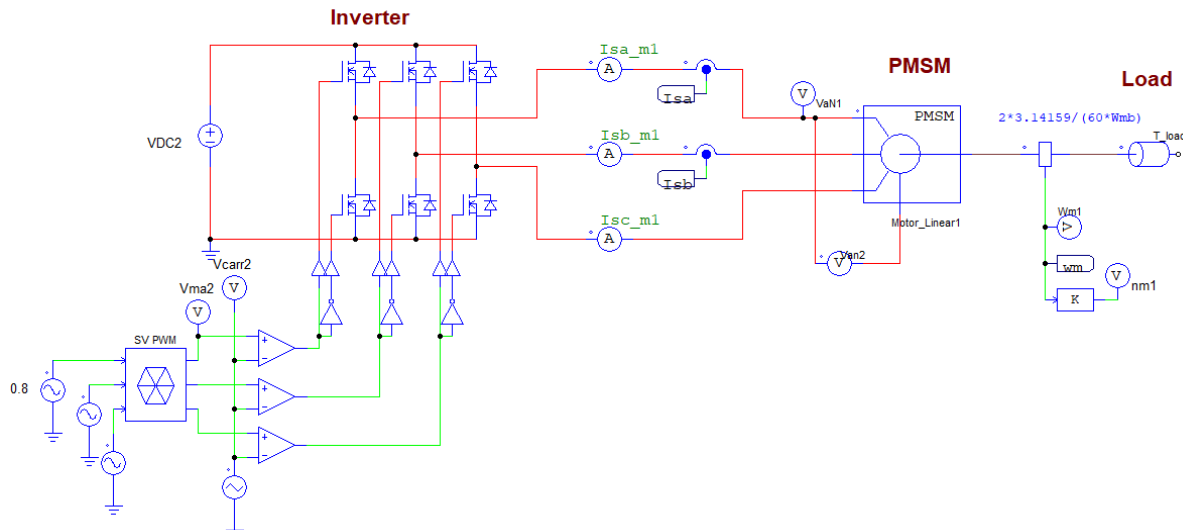
FIGURE 6. Three phase inverter SPWM.

In the circuit model, the battery can be modelled. A dependent voltage-controlled voltage source is used to represent the voltage source (VCVS). This is done because a fully charged battery cell has a higher voltage, which falls as the battery empties. A battery cell's state of charge (SOC) is expressed as a percentage ranging from 0% to 100% [23]. To account for the dynamic behavior of the cells, the equivalent series resistance (ESR) R_{batt} is added. The resistance, in particular, determines the voltage drop of the battery cell. When a load is present, Vbatt experiences a voltage decrease (i.e., Voc > Vbatt in loaded conditions). Q is denoted for total capacity, and i(t) stands for load current in amperes. The charge efficiency is defined as the total charge going out divided by the total charge coming in (η = Qdischarge / Qcharge). We can apply some integration and manipulation in the digital realm to change it to a discrete-time model rather than the continuous model previously given [23]. The open circuit voltage is a function of the SOC, according to these formulas. When the current is less than zero, as it is when the battery is charging, the terminal voltage is greater than the open circuit voltage, according to the formulas. The terminal voltage Vbatt is smaller than the open circuit voltage because the current in discharging mode is larger than zero. The battery model's parameters can be computed using (24) - (26). The voltage and capacity derating factors are Ks and Kp, respectively. The battery pack's Ns and Np represent the number of cells in series and parallel, respectively.

$$E_{rated\_total} = N_S \cdot K_S \cdot E_{rated} \qquad (24)$$

$$Q_{rated\_total} = N_p \cdot K_p \cdot Q_{rated} \qquad (25)$$

$$R_{battery\_total} = \frac{N_s}{N_p} \cdot R_{battery} \qquad (26)$$

For initial simulation parameters it can be assumed that the DC bus voltage is 500 V and a charge of 65 Ah. A starting point can be made for modeling the battery using these initial

simulation estimates for the battery pack. By referencing the datasheet of the chosen battery cell, the rated specifications can be obtained. For example, from Panasonic's 18650 lithium-Ion battery cell (NCR18650GA) datasheet the rated voltage of a cell is 3.6V with a capacity of 3300mAh. Therefore, using (24) – (25), an estimate of the number of cells can be made. The number of series cell to meet the initial simulation conditions would be $N_s = 139$ cells and for the parallel connections, $N_p = 20$ cells. However, the number of series cell can be reduced by reducing the output voltage and using a boost converter to obtain the desired output. Therefore, using an arbitrary voltage of 250 V, we can redesign the battery pack. This would give us $N_s = 70$ cells and $N_p = 20$ cells (since the capacity is not changing).

III. SIMULATION OF THE MOTOR CONTROLLER AND DRIVE SYSTEM

To implement the propulsion system PSIM software was used. The design was first implemented using a template provided by PSIM for electric vehicles traction motors. This template was used as a starting point and edited to suit the appropriate application. One of the most important components of the drive system is the three-phase inverter. Therefore, the first aspect to designing the traction motor is the inverter. Using IGBT blocks from the PSIM library, the two-level topology can be realized. The topology created in PSIM can be seen in Fig. 6. The switching signals are generated based on sinusoidal pulse width modulation theory. Three AC voltage sources were used each with 0.8 peak amplitude shifted by 120 degrees. The frequency for the reference AC signals were set to 60 Hz. These signals are compared with a triangular wave voltage source. The switching frequency was set to 10 kHz with approximately double the amplitude of the reference source. The resulting waveforms are shown in Fig. 7.
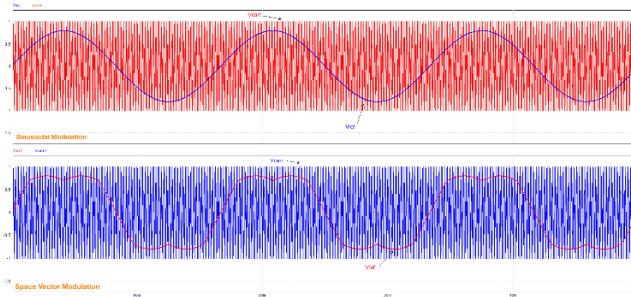
FIGURE 7. SPWM and SVPWM modulation scheme waveforms.

TABLE 3. AC sweep parameters.

Parameters	Value
Start Frequency	10 Hz
End Frequency	3 kHz
No. of Points	51 Points
Start Amplitude	1 V
End Amplitude	15 V

A. OPEN LOOP CONTROLLER DESIGN

The first step of implementing the drive system for the motor is simulating the proposed field-oriented control model in open loop conditions. This portion follows steps provided in [24]. Fig. 8 shows the setup done in PSIM. The motor and load parameters were given arbitrary values to first implement a working proof of concept controller. It includes a DC bus voltage, 6 IGBTs, a PM synchronous motor and the commanded control signals I_d and I_q. The waveforms for this circuit setup are given in Fig. 9. The three phase currents are shown in the first graph. I_d and I_q currents are shown in the second graph, the waveforms show that it reaches steady state. This can also be seen in the last graph for the velocity ω_m.

B. CURRENT CONTROLLER DESIGN

To design the controllers for the closed loop system for the inner current controllers, we can obtain the PI parameters by analyzing the frequency response of perturbed I_d and I_q. Fig. 10 shows the waveforms generated after perturbating I_q at incremented frequencies.

The results of this perturbation look as expected. Fig. 10 (a) had I_q perturbated at 1 V, 10 Hz. The current waveforms are distorted. We can see that the quadrature current follows the

oscillation well. Additionally, we can see that our modulation index is staying in the envelop of the carrier wave. As the frequency increases, we can see that the response of the I_q lowers. At 3kHz the perturbation is harder to observe as we are increasing the frequency. This required a change in the amplitude to 15 volts to obtain observable data. Now that the parameters are set and we can observe that the waveform during perturbation is as expected, we can perform the AC sweep. Table 3 shows the parameters for the AC sweep block in PSIM. The frequency response of the AC sweep is given in Fig. 11.

A similar process in observing the perturbed waveforms for I_d was performed. Using the frequency responses generated by the AC sweep, we can input it into SmartCtrl and obtain the PI values. This can be done easily with SmartCtrl's stable solution space/map. The solution space is generated based on the plant, sensor, and type of regulator the user sets. SmartCtrl then provides a map of stable region in a phase margin vs crossover frequency chart. Fig. 12 shows the controller designer in SmartCtrl. It includes the bode plots, polar plot, and the step response. The bode plots have two lines, the pink one is the control to output response and the green line is the open loop response. Using the Solution map control, we can pick between the phase margin and the cross frequency that
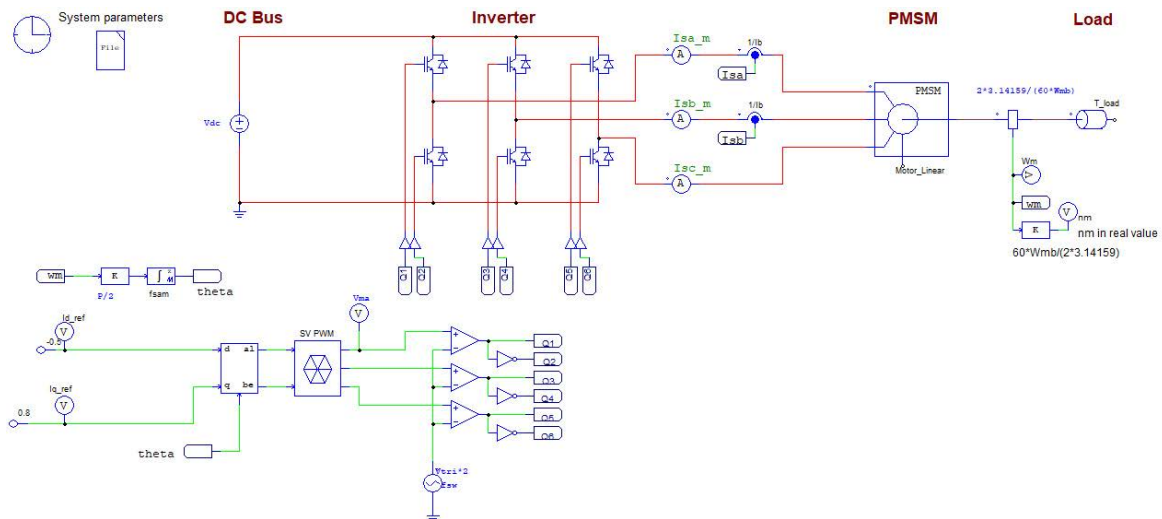

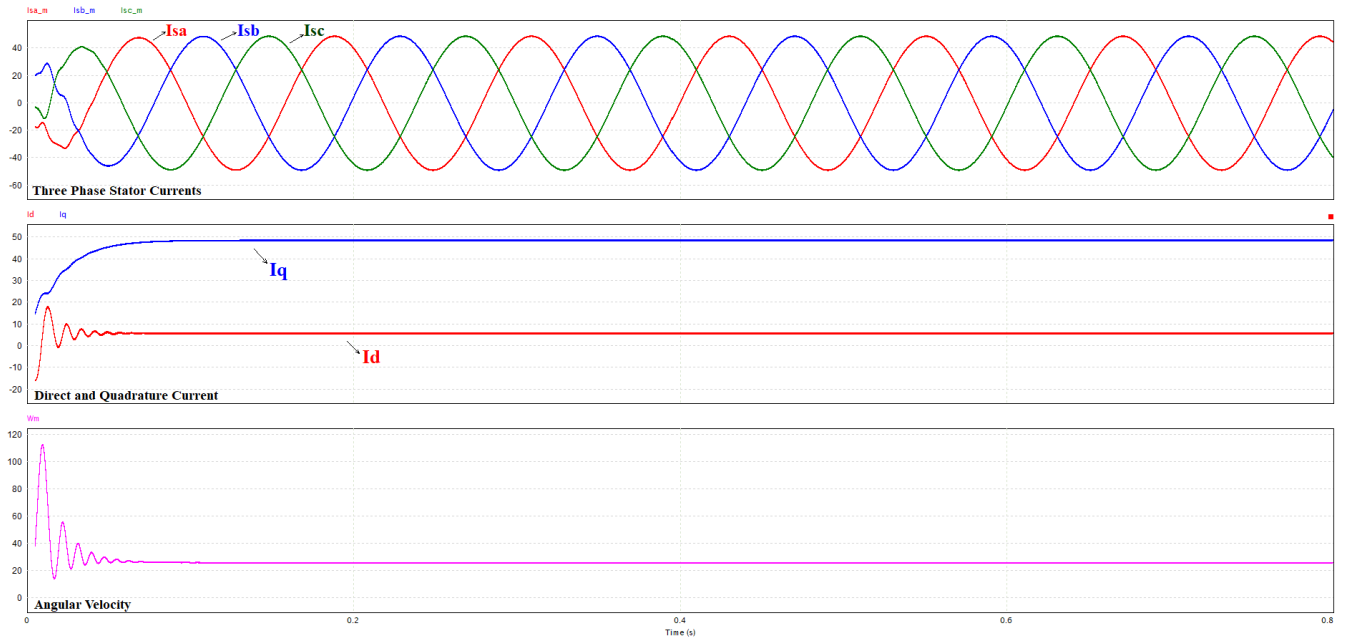**FIGURE 8.** Open loop PSIM setup of drive system.

FIGURE 9. Open loop simulation results.

TABLE 4. Control loop PI values.

Current Loop	Parameter	Value
I_q	K_i	16.2763
	$T_i(s)$	9.88305 [ms]
I_d	K_i	6.6574
	$T_i(s)$	4.6395 [ms]

FIGURE 11. Iq frequency response (AC sweep).

FIGURE 10. Perturbation in Iq at (a) 1 V, 10 Hz (b) 1 V, 100 Hz (c) 15 V, 3 kHz.
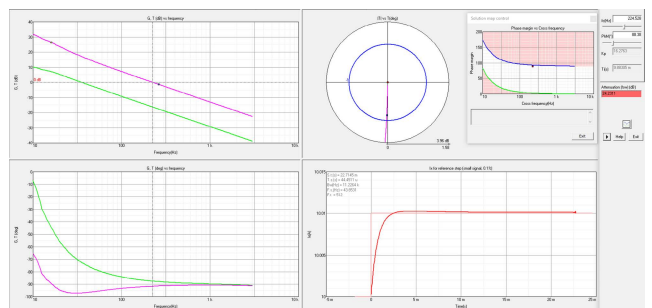
FIGURE 12. SmartCrtl results for open loop design.

provides a minimal overshoot and settles at an acceptable rate in the step response. After tuning the point in the solution map control to the desired step response, we can take the values of Kp and $T_i(s)$ for the PI controller for I_q. This process was repeated for I_d.

These parameters were placed into the PI controllers for the inner control loops. The control algorithm is shown in Fig. 13. The control circuit shows the newly added PI controllers for the I_q and I_d. A perturbation was added into the I_q reference signal. The generated waveforms are also shown in Fig. 13.

We can see from the first graph that the I_d reference is having a hard time to stabilize to zero. However, the peak-to-peak amplitudes are minimal. The next graph shows the I_q and I_q reference signals. We can see the I_q oscillating due to
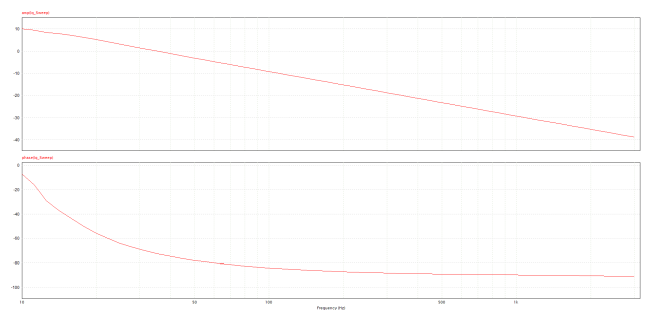
the perturbation and is following the reference well. The last graph shows the speed which is also oscillating as expected. This process was repeated for the speed loop. The overall closed loop simulation is provided in Fig. 14.

To reiterate, the PI paramter are designed using smartC-TRL. First a freqency sweep of the system is required, this provides the magnitiude and phase plot for smartCTRL.

FIGURE 13. Inner PI controller schematic and generated waveforms.

FIGURE 14. Waveforms after adding the speed controller (full load).

Using these plots, the software provides stable design points. Playing around with the corss frequency and phase marigin an instant view of the step response and control plots are provided. Thus, a designer can easily determine working values for their regulator. These values can then be used in the model to simulate and observe the response. The system

TABLE 5. Battery pack parameters.

Parameters	Value	Units
N_s - No. of cells in series	70	cells
N_p - No. of cells in parallel	60	cells
E_{rated} - Rated voltage	3.6	V
E_{cut} - Discharge cut-off voltage	2.5	V
Q_{rated} - Rated capacity	3.35	Ah

TABLE 6. Design specification for full integration.

Parameters	Value	Units
Input Voltage (V_{batt})	500	V
Output Voltage (V_{DC})	252	V
Switching Frequency (f_s)	50	kHz
Voltage Ripple ($\Delta V_c / V_o$)	3	%
Inductor Current Ripple ($\Delta I_l / I_o$)	5	%
Maximum Power (P_{max})	40	kW

can then be later tuned manually or by using other control thoery/tools to the obtain the desired performance.

C. SIMULATION OF THE BATTERY SYSTEM

To simulate the lithium-ion battery model, PSIM's implementation is used. To model the battery, the simulation uses Panasonic's line of 18650 lithium-Ion battery cell (NCR18650B). The specifications are filled out in Table 5.

These specifications were obtained through the datasheet, estimations based on other batteries with similar properties and obtaining values from the discharge curve of the battery. PSIM's curve capture functionality was used to extract key points from the discharge curve provided in the manufacturer datasheet. The number of cells in series and parallel were calculated using battery equations mentioned in the previous section. A 70s60p cell configuration will output 50 kW at 252 V. The gathered information from the datasheet can now be used to generate the lookup table for the battery model. The look up table battery model requires three inputs. The open circuit voltage vs. state of charge and the two internal resistances vs. the state of charge curves for both charging and discharging.

To generate the lookup tables, first, the PSIM provided example schematic in Fig. 15 was used. This schematic generates the open circuit voltage with respect to the state of charge. Additionally, the same circuit is used to obtain the internal resistance curves for discharging case.

To generate the charging resistance vs. SOC table, the schematic in Fig. 16, provided by PSIM was used.
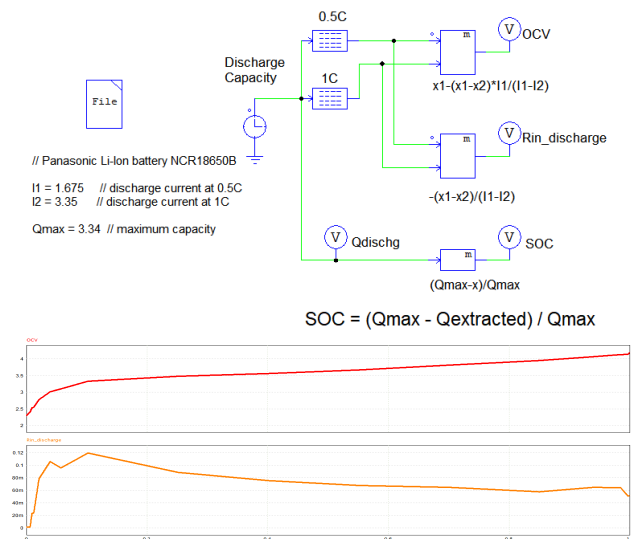
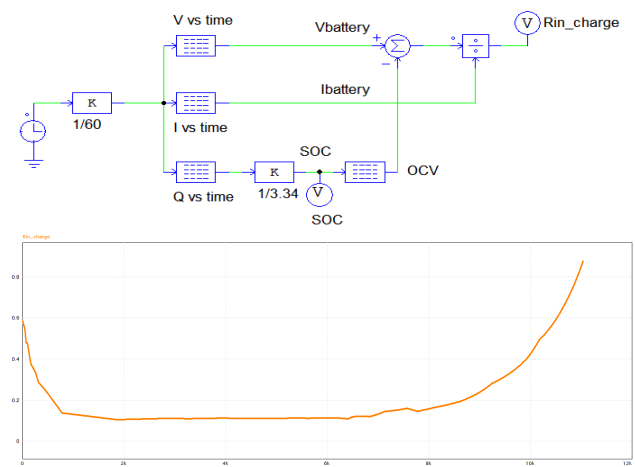**FIGURE 15.** OCV and Rin vs. SOC discharge curves for the NCR18650B.

FIGURE 16. Rin vs. SOC charge circuit setup and output curve for the NCR18650B.

After setting the initial settings, the battery parameters were fine-tuned using charging and discharging tests described in [25] and observing the characteristics. The charge test simulation in Fig. 17 shows that at 0.5C it takes around 3 hours to reach 100% state of charge. Fig. 18(a) shows the discharging test bed of the battery model. The setup includes the battery, which is modeled using the parameters in Table 5 (for one cell), probes to measure the state of charge, battery voltage, battery current and the capacity amp-hour (which is simulated using $Q = I_{discharge} \cdot t_{hours}$). The simulation results for the discharging test are given in Fig. 18 (b). Lastly, the testing for the charging circuit was simulated as shown in Fig. 19. In conclusion, the model is working as intended. The discharge and charge curves match closely to
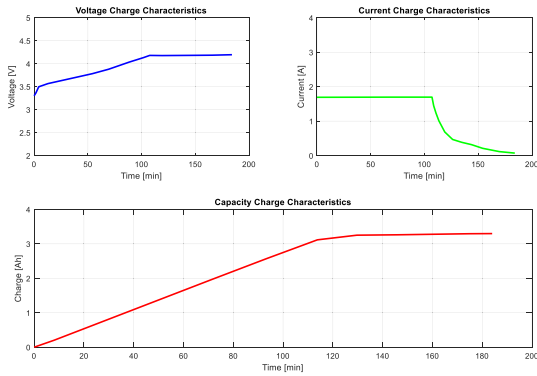
FIGURE 17. Charge characteristics for the NCR18650B.

the one described in the datasheet. Moreover, the constant current and constant voltage charging region can be easily seen. This model can now be used in the overall simulation for the Hyperloop.

D. SIMULATION OF THE FULL INTEGRATION

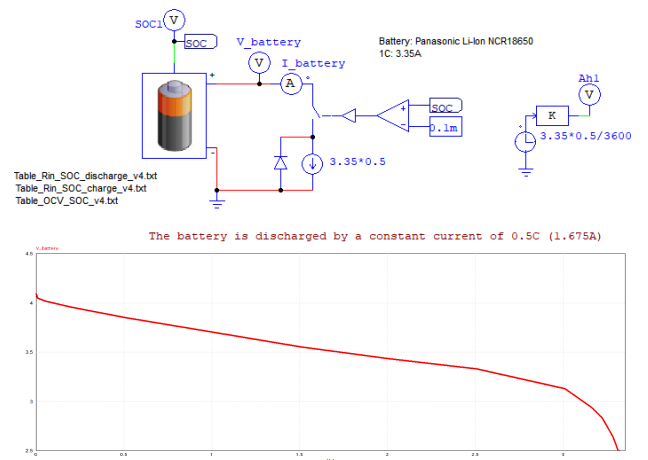The full integration of all the components used is shown in Fig. 20. The lithium-ion battery module, bi-directional

FIGURE 18. Discharge test for NCR18650B model.

DC-DC converter, three-phase inverter, and permanent magnet synchronous motor make up the power side, as shown. The control side includes the field-oriented control blocks along with PSIM's charge/discharge algorithms for the DC/DC converter. Looking at the initial results shown in
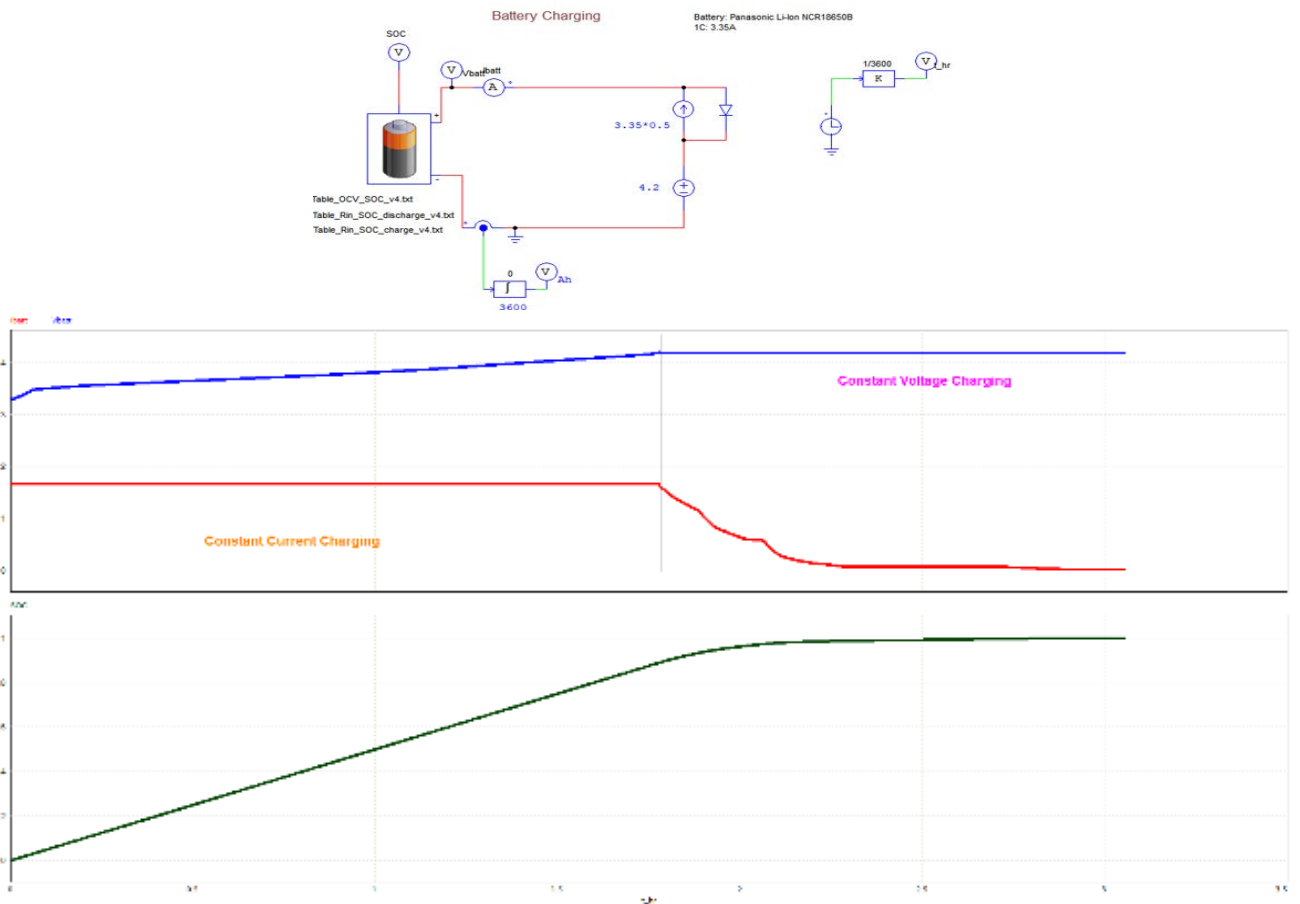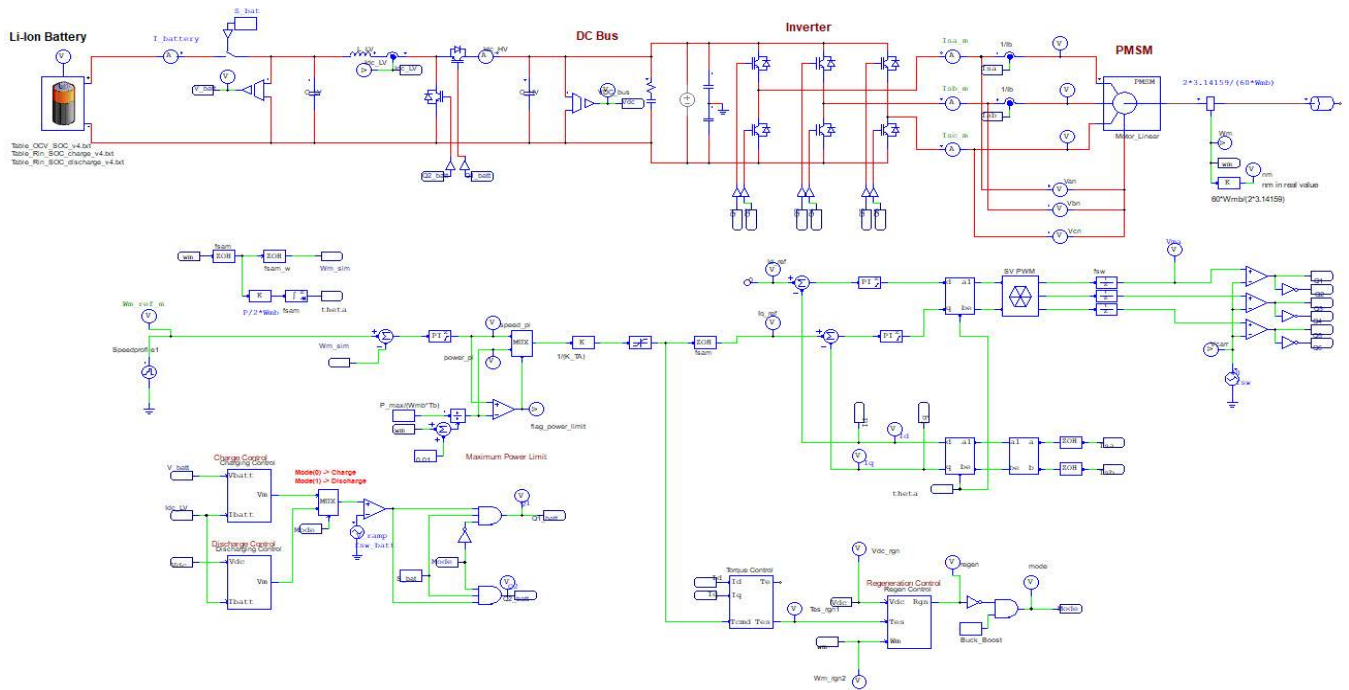

FIGURE 19. Charge test for NCR18650B model.

FIGURE 20. Complete setup for the Hyperloop LSM propulsion system (based on PMSM).

TABLE 7. Additional simulation parameters.

Model	Parameters	Value	Units
Motor	Stator Resistance (Rs)	4.3	Ohms
	d-axis inductance (Ld)	0.027	V
	d-axis inductance (Lq)	0.067	kHz
	Back EMF Vpk/krpm (Ke)	98.67	V/RPM
	Poles (P)	4	-
	Maximum Power (P$_{max}$)	40	kW
DC/DC Converter	Buck Current controller	Kp = 0.06 Ki = 0.0005	-
	Buck Voltage Controller	Kp = 2.0106176 Ki = 0.00099472	-
	Boost Current Controller	Kp = 0.04 Ki = 0.0005	-
	Boost Voltage Controller	Kp = 0.57805 Ki = 0.0009	-

Fig. 21 (a), the three phase AC currents, at starting, is 10 amps peak to peak which then settles down to around 7 amps peak to peak. The battery voltage and current are as expected. The average battery voltage at 80% SOC is 272 V and the average battery current drawn is 6.7 A. The boosted DC voltage seem sporadic which may need further investigations. However, the
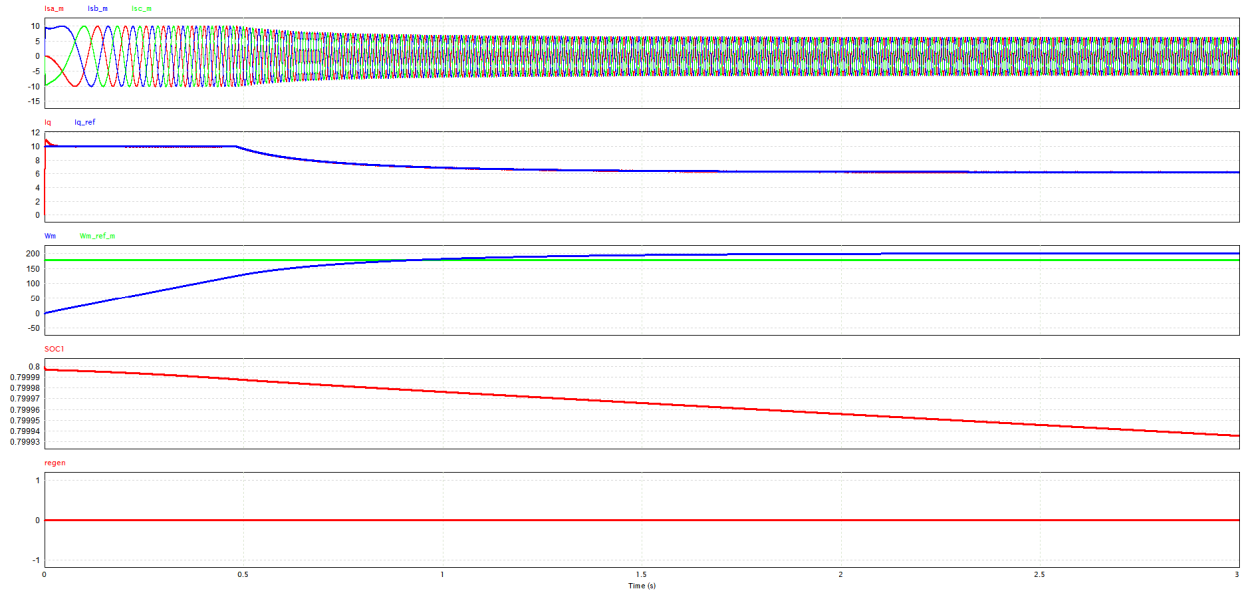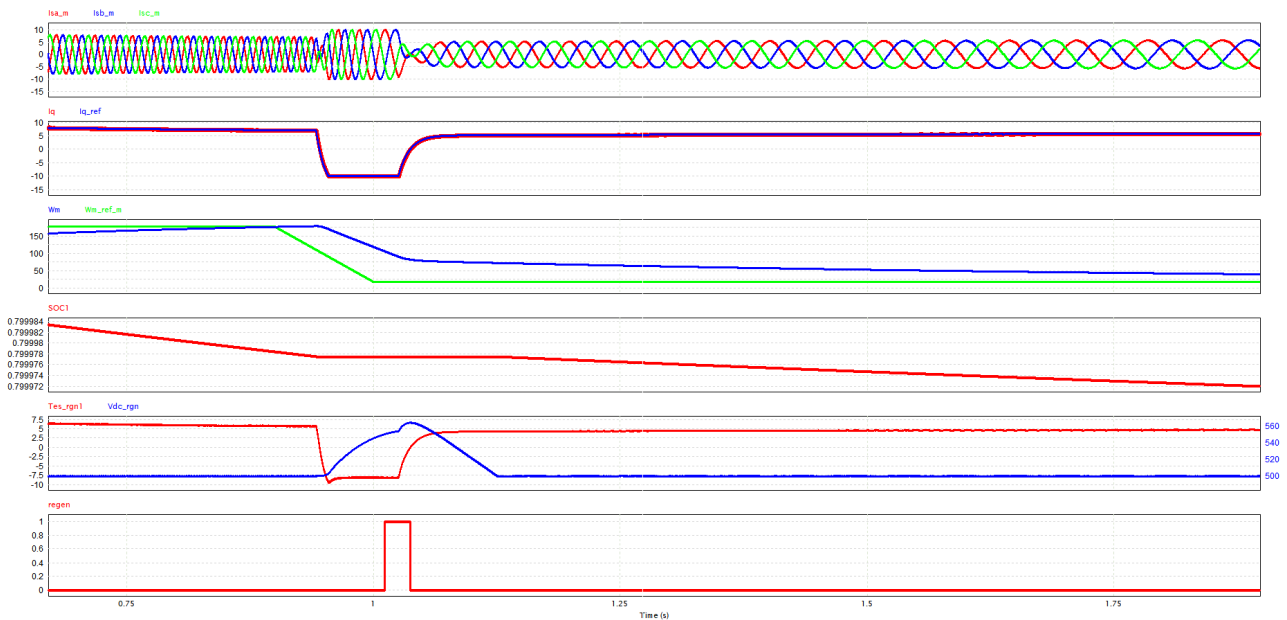
FIGURE 21. Motoring mode operation results.

FIGURE 22. Regenerative braking operation results.

average voltage is as expected of 500 V with a small ripple as shown in Fig. 21 (b). The control signals and their references can be compared and studied in Fig. 21 (c). The Id was set to 0, the measured signal oscillates with an average of 22 mA.

The Iq follows the reference well and achieves steady state before t = 0.2 s. Finally, the speed ramps up to the set reference by t = 0.9 s. The simulation triggered the power limiter which means some parametrization may be under specified. To test the motoring and generating mode of operations, first the motor speed profile is set to run with a constant speed. The waveform in Fig. 21 shows that the machine is in motoring mode of operation and through the

SOC waveform, the battery can be seen discharging at the expected rate. Then, to show the regenerative braking, the reference speed profile is adjusted to drop in speed at a certain instant and then back to the nominal reference. Fig. 22 shows the regenerative braking mode of operation. The controller achieves promising performance results as steady the transient at startup lasts less than a couple milliseconds. The linear speed reached 280 m/s drawing around 40 kW of power.

It is important to note that the design is based around a small prototype system thus the power requirement and motor design would change significantly for a passenger car-
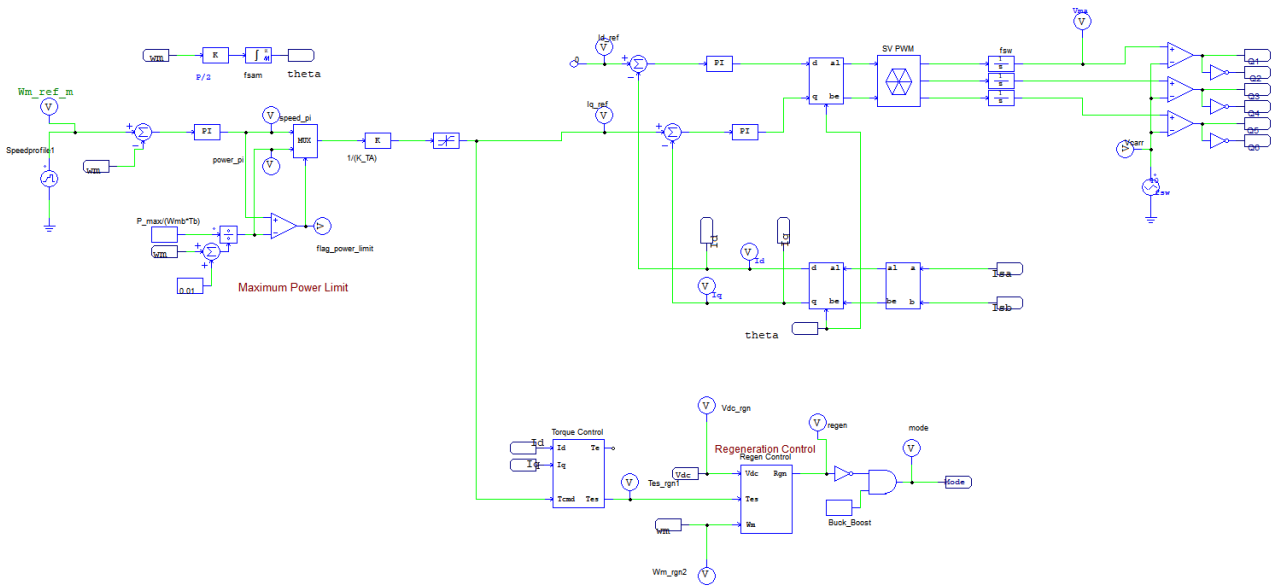
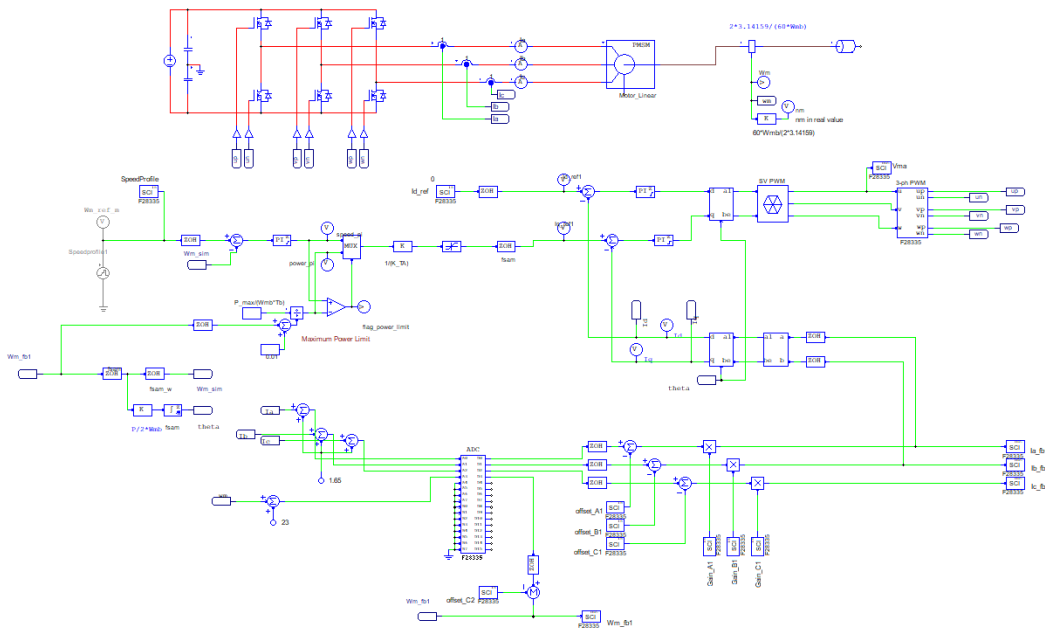**FIGURE 23.** PSIM controller update to account for digital delay.

FIGURE 24. PSIM schematic for TI DSP.

rying, full sized Hyperloop. The main simulation parameters not previously provided is summarized in Table 7. Additional parameters not shown used default values provided by PSIM.

IV. HARDWARE IN THE LOOP SIMULATION
The online hardware in the loop setup requires the use of a DSP with the control algorithm (imported from PSIM) and the Typhoon HIL box. Before uploading the controller algorithm from PSIM, the design needs to be slightly adjusted

for digital control. Thus, new digital blocks are appropriately used. The delay blocks are used to simulate the update cycles of a real microcontroller/DSP. Moreover, in a real system the sensors would sample it in discrete values, thus the discretization is simulated using zero-order hold blocks. Fig. 23 shows the PSIM controller setup for digital control. Fortunately, the impact of the digital delay was minimal and the original PI values were used. This means the phase margin stayed relatively the same. Fig. 24 shows the updated schematic to generate the C – code for the Texas Instrument DSP. Some
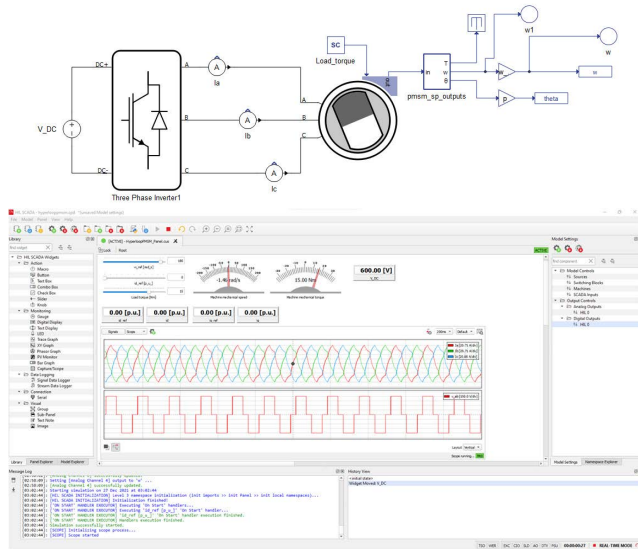
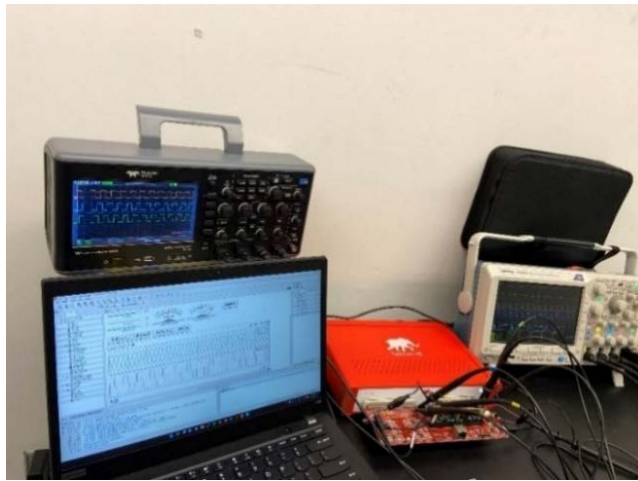**FIGURE 25.** Typhoon HIL – real time simulation schematic and SCADA setup.

FIGURE 26. Hardware in the loop setup.

FIGURE 27. Four pulse width modulation signals generated by TI DSP.
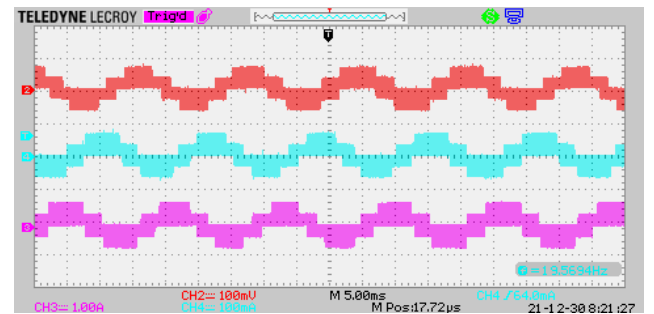
FIGURE 28. Line – to – neutral voltage waveforms.

FIGURE 29. Three – phase motor currents.

new blocks were introduced to facilitate the integration of the DSP and Typhoon HIL. This includes the TI analog to digital converter block and the 3 – phase DSP PWM generator block.

After generating the embedded code for the DSP, code composer studio was used to upload it into the TI card. Once the DSP was turned on, the PWM signal generated in no load conditions was seen on the oscilloscope. Next the Typhoon HIL model was loaded, the real time simulation setup is provided in Fig. 25. This model in Typhoon does not use any of the input control elements and only contains the power and signal outputs from the motor. The modulation was mapped internally to the appropriate pins from the DSP.

The real time setup for hardware testing of the DSP is provided in Fig. 26. The setup includes the PC debugging the CCS and Typhoon HIL code, Typhoon 402 HIL box,
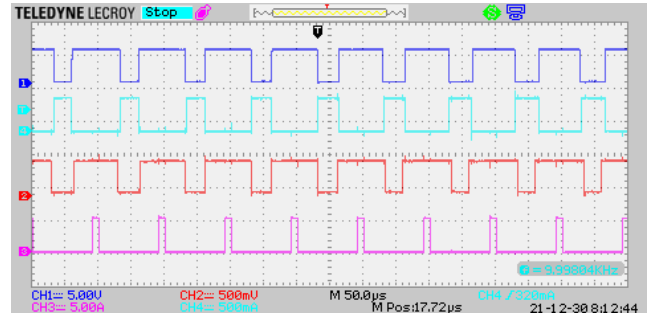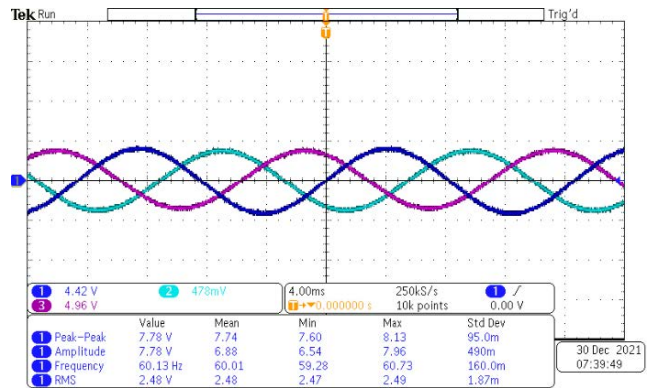
TI F28335 DSP. The scope on the left shows the PWM signals from the DSP, and the scope on the right shows the three – phase currents. The control setup is providing and receiving real digital signals. The motor and power side are the only portion that is virtual. The real time results can be observed by measuring the I/O signals from the Typhoon HIL hardware.

The following figures show the resulting oscilloscope waveforms from HIL simulations. Figure 27 illustrates pulse width modulating signals generated by the TI DSP control card. The dark blue, red and pink waveforms are the PWM waves for each leg of the inverter. Additionally, one out the three inverting PWM signal is shown in light blue. As expected, the wave is inverted to the first PWM signal with the pre-set duty cycle of 0.5us.
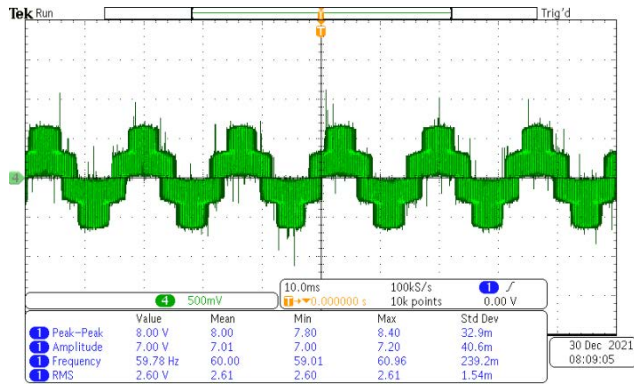
FIGURE 30. Three - phase line – to – neutral voltage waveforms.

The three-phase line to neutral voltage waveforms are provided in Fig. 28. This is the analog signal outputted by the HIL 402 box from Typhoon HIL software. The values are scaled down from the digital to analog converter. The three phase currents are shown in Fig. 29 and finally another line to neutral voltage for phase a and b is shown in Fig. 30.

V. CONCLUSION

Prior to this work there has only been some design studies for the Hyperloop. Moreover, there has never been a methodology on how to design such a system. The methodology used in this paper uses similar process in designing electric vehicles. The design is first simulated offline, then it is recreated and simulated in a real - time hardware in the loop environment. This methodology provides a significant cost efficient, time conscience design process, before taking on the big step in building a full prototype. The financial costs to build a real Hyperloop system would be billions of dollars. Even with a lab prototype, the cost would require a large investment of hundreds of thousands of dollars. Thus, in the interest of time and money, it would be wise to first model, simulate and emulate the system in real time using HIL technology such as Typhoon HIL.

This paper provides, for the first time, a significant step forward towards the development of such a revolutionary system and provides a relatively simple process, cost effective and less time-consuming methodology of judging any futuristic Hyperloop design. In addition, all previous systems reported so far are still in development or never deployed in the market; most of them are Linear Induction Motors (LIM). The study provides a design based on Linear Synchronous Motor (LSM) which is fast and reliable at high speeds. Not only does this paper provide a sound modelling system for the propulsion but goes the extra mile by testing it in another environment. The simulation from PSIM and Typhoon HIL are both in agreement. This was done to verify that the effort put into the modelling and design of such system is correct. The overall HIL simulation provided sound results from the propulsion design and an accurate real time operation of the system.

The main contribution of this paper is to study the novel concept of the Hyperloop system and its propulsion challenges. This included studying the advantages and disadvantages of different power and control topologies. The contribution of the design pertains to the first-time integration of multiple components regarding the Hyperloop propulsion. Additionally, there is a research gap for the Hyperloop technology. Thus, the paper provides an overview of the modeling and design of the propulsion system in the various top of the line software's (PSIM, Simulink & Typhoon HIL) for the first time. More specifically, this is the first time a design methodology, simulation, and modeling for a Hyperloop propulsion system using linear synchronous motors was demonstrated. The contribution of this paper was to provide insight to a Hyperloop propulsion system built in closed loop form, and the design process using PSIM and verifying it in Typhoon HIL. The paper focused mainly on the propulsion system. Moreover, the design focused on a simulating for a small-scale laboratory model. Thus, there are some limitations on the design for a real Hyperloop such as the power requirements for a full system compared to just the propulsion system, a larger propulsion motor would call for a different inverter configuration, etc. However, this would be a topic for a future paper covering the hardware prototype. This research hopes to promote and fill the research gap. Evidence of successful implementation of this design in both PSIM and Typhoon HIL is shown. With the use of the various tools (PSIM & SmartCtrl, Simulink, and Typhoon HIL), a successful steppingstone for a Hyperloop propulsion system was realized. Overall, the purpose of this study is to continue promoting and provide the foundation for further development of such a novel transportation system. Future work for this study includes building a laboratory prototype of the hardware. This will be built in confidence through the methodology described in this paper.

REFERENCES

[1] SpaceX. (2013). *Hyperloop Alpha*. [Online]. Available: https://www.tesla.com/sites/default/files/blog_images/hyperloop-alpha.pdf

[2] B. Kowal, R. Ranosz, M. Klodawski, R. Jachimowski, and J. Piechna, "Demand for passenger capsules for hyperloop high-speed transportation system—Case study from Poland," *IEEE Trans. Transport. Electrific.*, vol. 8, no. 1, pp. 565–589, Mar. 2022, doi: 10.1109/TTE.2021.3120536.

[3] A. Tbaileh, M. Elizondo, M. Kintner-Meyer, B. Vyakaranam, U. Agrawal, M. Dwyer, and N. Samaan, "Modeling and impact of hyperloop technology on the electricity grid," *IEEE Trans. Power Syst.*, vol. 36, no. 5, pp. 3938–3947, Sep. 2021, doi: 10.1109/TPWRS.2021.3056298.

[4] J. Lim, J.-H. Jeong, C.-H. Kim, C.-W. Ha, and D.-Y. Park, "Analysis and experimental evaluation of normal force of linear induction motor for maglev vehicle," *IEEE Trans. Magn.*, vol. 53, no. 11, pp. 1–4, Nov. 2017, doi: 10.1109/TMAG.2017.2699694.

[5] J.-H. Jeong, J. Lim, C.-W. Ha, C.-H. Kim, and J.-Y. Choi, "Thrust and efficiency analysis of linear induction motors for semi-high-speed Maglev trains using 2D finite element models," in *Proc. IEEE Conf. Electromagn. Field Comput. (CEFC)*, Nov. 2016, p. 1, doi: 10.1109/CEFC.2016.7816093.

[6] S. Jacobs, J. Rens, E. Di Silvestro, and G. Sellitto, "Electromagnetic aspects of the structural integration of linear synchronous machines for a hyperloop technology," in *Proc. 13th Int. Symp. Linear Drives Ind. Appl. (LDIA)*, 2021, pp. 1–6, doi: 10.1109/LDIA49489.2021.9505748.

[7] C. Y. Lee, J. Lee, J. H. Lee, J. M. Jo, C. B. Park, W. H. Rue, Y. D. Chung, Y. J. Hwang, T. K. Ko, and S.-Y. Oh, "Conceptual design of superconducting linear synchronous motor for 600-km/h wheel-type railway," *IEEE Trans. Appl. Supercond.*, vol. 24, no. 3, pp. 1–4, Jun. 2014, doi: 10.1109/TASC.2013.2284662.

[8] H. Wang, J. Li, R. Qu, J. Lai, H. Huang, and H. Liu, "Study on high efficiency permanent magnet linear synchronous motor for maglev," *IEEE Trans. Appl. Supercond.*, vol. 28, no. 3, pp. 1–5, Apr. 2018, doi: 10.1109/TASC.2018.2796560.

[9] R. J. K. Masada and E. Masada, "Comparison of linear synchronous and induction motors," Federal Transp. Authority, Washington, DC, USA, Tech. Rep. FTA-DC-26-7002.2004.01, 2004. [Online]. Available: https://www.codot.gov/programs/research/pdfs/2004/inductionmotors.pdf

[10] A. R. Sadat, H. Shadabi, M. Sabahi, and M. B. B. Sharifian, "Tracking of X-Y direction positions with using permanent magnet linear synchronous motors," in *Proc. 22nd Iranian Conf. Electr. Eng. (ICEE)*, May 2014, pp. 527–532, doi: 10.1109/IranianCEE.2014.6999600.

[11] K. Wang, Q. Ge, L. Shi, Y. Li, and Z. Zhang, "Development of ironless Halbach permanent magnet linear synchronous motor for traction of a novel Maglev vehicle," in *Proc. 11th Int. Symp. Linear Drives Ind. Appl. (LDIA)*, Sep. 2017, pp. 1–5, doi: 10.23919/LDIA.2017.8097238.

[12] P. Sun, Q. Ge, B. Zhang, and Z. Gao, "An improved sensorless control method for long stator linear synchronous motor," in *Proc. 22nd Int. Conf. Electr. Mach. Syst. (ICEMS)*, Aug. 2019, pp. 1–4, doi: 10.1109/ICEMS.2019.8922404.

[13] J. Jin, H. Zhao, Y. Xin, and Y. Sun, "Simulation and analysis of a PMLSM control system based on SVPWM," in *Proc. 29th Chin. Control Conf. (CCC)*, vol. 10, 2010, pp. 3316–3320.

[14] D. Chen, Y. Huang, S. Chen, and S. Lu, "A simulation model of PMLSM based on physical platform," in *Proc. 33rd Chin. Control Conf.*, Jul. 2014, pp. 6555–6559, doi: 10.1109/ChiCC.2014.6896074.

[15] L. Xu, R. Wei, Q. Ge, X. Wang, and Y. Li, "Hardware-in-loop simulation of linear synchronous motor based on three-level converter," in *Proc. Int. Conf. Electr. Mach. Syst. (ICEMS)*, Oct. 2013, pp. 1944–1947, doi: 10.1109/ICEMS.2013.6713218.

[16] C. You, R. Zhang, X. Wang, Y. Du, and Q. Ge, "Vector control of maglev PMLSM based on minimum loss SVPWM method," in *Proc. 19th Int. Conf. Electr. Mach. Syst. (ICEMS)*, 2016, pp. 1–4.

[17] W. Zhao, S. Jiao, Q. Chen, D. Xu, and J. Ji, "Sensorless control of a linear permanent-magnet motor based on an improved disturbance observer," *IEEE Trans. Ind. Electron.*, vol. 65, no. 12, pp. 9291–9300, Dec. 2018, doi: 10.1109/TIE.2018.2823660.

[18] J. F. Gieras, Z. J. B. Piech, and B. Tomczuk, *Linear Synchronous Motors: Transportation and Automation Systems*. Boca Raton, FL, USA: Taylor and Francis, 2011.

[19] I. Boldea, *Linear Electric Machines, Drives, and Maglevs Handbook*. 2017.

[20] *Field Orientated Control of 3-Phase AC-Motors*, Texas Instruments, Dallas, TX, USA, 1998.

[21] J. S. Lai and D. J. Nelson, "Energy management power converters in hybrid electric and fuel cell vehicles," *Proc. IEEE*, vol. 95, no. 4, pp. 766–777, Apr. 2007, doi: 10.1109/JPROC.2006.890122.

[22] PSIM. (2016). *HEV Design Suite*. [Online]. Available: https://psim.powersimtech.com/hubfs/PDF%20Tutorials/Tutorial%20-%20HEV%20Design%20Suite.pdf

[23] G. L. Plett, *Battery Management Systems: Battery Modeling*, vol. 1. Norwood, MA, USA: Artech House, 2015.

[24] PSIM. (2014). *How to Implement Field Oriented Control of PMSM With PSIM & SmartCtrl*. [Online]. Available: https://powersimtech.com/resources/tutorials/how-to-implement-field-oriented-control-of-pmsm-with-psim-smartctrl/

[25] PSIM. (2016). *Lithium-Ion Battery Model*. [Online]. Available: https://powersimtech.com/resources/tutorials/lithium%E2%80%90ion-battery-model/

MOHAMMAD ABDUL BHUIYA (Member, IEEE) received the bachelor's degree in electrical engineering from the Institute of Technology (Ontario Tech University), University of Ontario, Oshawa, ON, Canada, in 2019, and the M.A.Sc. degree in electrical and computer engineering from Ontario Tech University, in February 2022. He is currently a Diagnostics Engineer at General Dynamics Land Systems (GDLS), London, ON, Canada. He is also a member of the Power Electronics and Drive Applications Laboratory (PEDAL). His research interests include power electronics, electric vehicle drives, and hyperloop transportation.

MOHAMED Z. YOUSSEF (Senior Member, IEEE) received the Ph.D. degree in power electronics from the ePEARL Laboratory, Queen's University, Canada, in 2005. He was later an Adjunct Assistant Professor involved in teaching and research. In 2007, he joined Bombardier Transportation, where he worked as a Senior Research and Development Engineer. In 2012, he joined Alstom Transport as a Research and Development Engineering Manager. He was the Motor and Electronics Manager of Armstrong Pumps before coming back to Academia. He is currently an Associate Professor with the ECSE Department, Institute of Technology (UOIT), University of Ontario, Canada. He is also the Director of the Power Electronics and Drives Laboratory (PEDAL), UOIT, and the University's Leader of the Space-X Team. He has more than 80 papers in the top tier IEEE journals and conferences with seven U.S./Canadian patents. His research interests include electromechanical systems for the transportation industry, electromagnetic compatibility (EMC) for the railways, and power electronics applications for the information technology. He is a fellow of the Canadian Council of Professional Engineers. He is a Professional Engineer in ON. He serves as the Co-Chair of the IEEE IES Toronto Section. He is an appointed Adjunct Professor at the Royal Military College (RMC) of Canada. He is a member of the IEEE Committee of Transportation Standards and a fellow expert of the Canadian government on many future infrastructure directives. He was recently appointed to the Consultancy Board of Sustainable Development Technology Canada (SDTC). He is also a member of the Egyptian Syndicate of Engineering. For more information visit the link (https://engineering.ontariotechu.ca/research/researchlabs/pedal.php).

• • •